



1           **Distribution of the Earth's radiation belts protons over the drift**  
2           **frequency of particles**

3                           **Alexander S. Kovtyukh**

4           Skobeltsyn Institute of Nuclear Physics, Moscow State University, Moscow, 119234, Russia

5           Correspondence: Alexander S. Kovtyukh (kovtyukhas@mail.ru)

6           **Abstract.** On the base of generalized data on the proton fluxes of the Earth's radiation belts  
7           (ERB) with energy from  $E \sim 0.2$  MeV to 100 MeV at drift shells  $L$  from  $\sim 1$  to 8, constructed  
8           stationary distributions of the ERB protons over the drift frequency  $f_d$  of protons around the  
9           Earth. For this, direct measurements of proton fluxes of the ERB in the period 1961–2017 near  
10           the plane of the geomagnetic equator were used. The main physical processes in the ERB  
11           manifested more clearly in these distributions, and for protons with  $f_d > 0.5$  mHz at  $L > 3$   
12           distributions of the ERB protons in the space  $\{f_d, L\}$  have a more orderly form than in the space  
13            $\{E, L\}$ . It has been found also that the quantity of the ERB protons with  $f_d \sim 1$ –10 mHz at  $L \sim 2$   
14           does not decrease, as for protons with  $E > 10$ –20 MeV (with  $f_d > 10$  mHz), but increases with an  
15           increase in solar activity. This means that the balance of radial transport and losses of the ERB  
16           low-energy protons at  $L \sim 2$  is disrupted in advantage of transport: for these protons, the effect of  
17           an increase in the radial diffusion rates with increasing in solar activity overpowers the effect of  
18           an increase in the density of the dissipative medium.

19

20

21           **Keywords.** Magnetospheric physics (energetic particles, trapped). Radiation belts.

22



## 23 1 Introduction

24 The Earth's radiation belts (ERB) consist mainly of charged particles with energy from  $E \sim 100$   
25 keV to several hundreds of megaelectronvolt (MeV). In the field of the geomagnetic trap, each  
26 particles of the ERB with energy  $E$  and equatorial pitch-angle  $\alpha_0$  ( $\alpha$  is the angle between the local  
27 vector of the magnetic field and the vector of a particle velocity) makes three periodic movements:  
28 Larmor rotation, oscillations along the magnetic field line, and drift around the Earth (Alfvén and  
29 Fälthammar, 1963; Northrop, 1963).

30 Three adiabatic invariants ( $\mu$ ,  $K$ ,  $\Phi$ ) correspond to these periodic motions of trapped particles,  
31 as well as three periods of time or three frequencies: a cyclotron frequency  $f_c$ , a frequency of  
32 particle oscillations along the magnetic field line  $f_b$ , and a drift frequency of particles around the  
33 Earth  $f_d$ . For the near-equatorial ERB protons, these frequencies belong to the following ranges:  $f_c$   
34  $\sim 1\text{--}500$  Hz,  $f_b \sim 0.02\text{--}2$  Hz and  $f_d \sim 0.1\text{--}20$  mHz. The frequency  $f_c$  increases by tens to hundreds of  
35 times with the distance of the particle from the plane of the geomagnetic equator (in proportion to  
36 the local induction of the magnetic field), and the frequency  $f_b$  decreases by almost 2 times with  
37 increasing the amplitude of particles oscillations.

38 The frequency  $f_c$  is different for different  $L$ -shells (near the equatorial plane) and as  $L$  increases  
39 it refers to an insignificant number of particles at higher and higher geomagnetic latitudes. Each  
40 given value of the frequency  $f_b$  with increasing  $L$  correspond to particles of more and more higher  
41 energies ( $E \propto L^2$ ) and it value encompass fewer and fewer particles.

42 Compared to the frequencies  $f_c$  and  $f_b$ , the drift frequency  $f_d$  of the ERB particles of one species  
43 belongs to a much narrower range; the frequency  $f_d$  does not depend on the mass of particles and  
44 very weakly depends on the amplitude of their oscillations (vary within  $\sim 20\%$ ). Herein, on each  $L$ -  
45 shell of the ERB there are a significant number of particles corresponding to a certain value of  $f_d$   
46 from a narrow frequency range.

47 Therefore, it can be expected that the distributions of the ERB particles in the space  $\{f_d, L\}$  will  
48 have a more orderly shape than in the space  $\{E, L\}$ , and the main physical processes in the ERB  
49 will manifest themselves more clearly in these distributions. It can also be expected that on these  
50 more ordered background will reveal more fine features of the ERB that do not appear in the space  
51  $\{E, L\}$ .

52 Meanwhile, despite the importance of the drift frequency  $f_d$  for the mechanisms of the ERB  
53 formation, reliable and sufficiently complete distributions of the ERB particles over the frequency  
54  $f_d$  have not been presented and these distributions have not been analyzed. This is the first time this  
55 is done here.

56 For greater reliance, this analysis is limited here to the protons of the ERB and it is refer to the  
57 magnetically quiet periods of observations, when the fluxes of the ERB protons and their spatial-  
58 energy distributions were stationary.

59 In the following sections, the distributions of the ERB protons over their drift frequency  $f_d$  were  
60 constructed by the experimental data (Sect. 2), and these distributions were analyzed (Sect. 3).  
61 Finally, the main conclusions of this work are given in Sect. 4.

## 62 2 Constructing the distributions of the ERB protons over their drift frequency

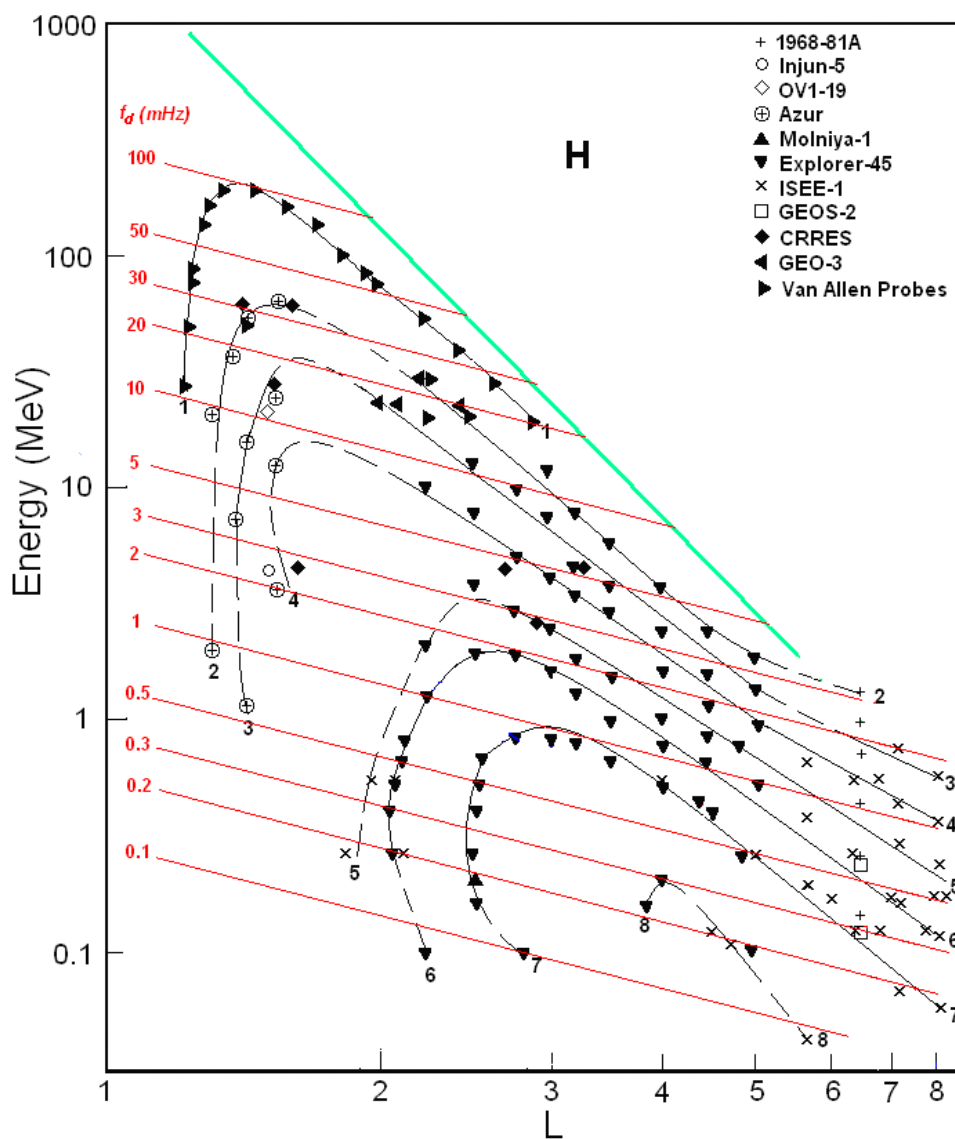
### 63 2.1 Spatial-energy distributions of the ERB protons near the equatorial plane

64 To construct the distributions of the ERB particles over the drift frequency, it is necessary to have  
65 reliable distributions of the differential fluxes of the ERB protons in the space  $\{E, L\}$ , where  $E$  is  
66 the kinetic energy of protons and  $L$  is the drift shell parameter.



67 According to the data of generalized and averaged satellite measurements of the differential  
 68 fluxes of protons with an equatorial pitch-angle  $\alpha_0 \approx 90^\circ$ , such distributions of proton fluxes for  
 69 quiet conditions is constructed in (Kovtyukh, 2020). Such distributions, separately for the periods  
 70 near minima and near maxima of the 11-year cycles of solar activity, is constructed from the  
 71 satellite data also for other main ionic components of the ERB near the plane of the geomagnetic  
 72 equator, but the most reliable and detailed picture was obtained in (Kovtyukh, 2020) for a protons.  
 73 In Fig. 1 one of these distributions is reproduced, for periods near maxima of the solar activity  
 74 (from 1968 to 2017).

75 Data of satellites are associated in Fig. 1 with different symbols. The numbers on the curves  
 76 (iso-lines) refer to the values of the decimal logarithms of the differential fluxes  $J$  ( $\text{cm}^2 \text{ s sr MeV}^{-1}$ )  
 77 of protons (with equatorial pitch-angle  $\alpha_0 \approx 90^\circ$ ). The red lines in Fig. 1 corresponds to the  
 78 dependences  $f_d(\text{mHz}) = 0.379 \cdot L \cdot E(\text{MeV})$  for the drift frequency of the near-equatorial protons in the  
 79 dipole approximation of the geomagnetic field.





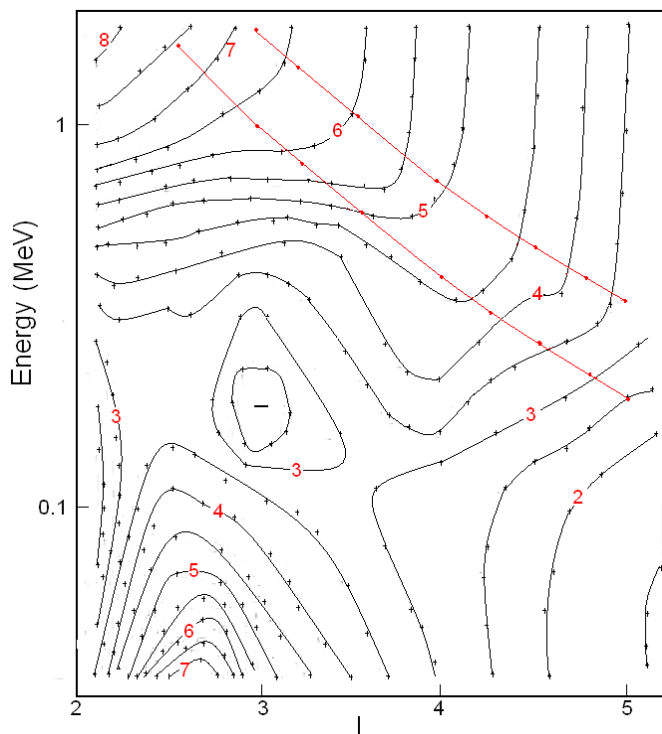
81 **Figure 1.** Distribution of the differential fluxes  $J(E, L)$  in the space  $\{E, L\}$  for protons with  $\alpha_0 \approx 90^\circ$  near maxima of  
 82 the solar activity (Kovtyukh, 2020). Data of satellites are associated with different symbols. The numbers on the  
 83 curves refer to the values of the decimal logarithms of  $J$ . Fluxes is given in units of  $(\text{cm}^2 \text{ s sr MeV})^{-1}$ . The red lines  
 84 corresponds to the drift frequency  $f_d$  (mHz). The green line corresponds to the maximum energy of the trapped protons.

85 On the drift shells can be trapped only protons with energies less than some maximum values,  
 86 determined by the Alfvén's criterion:  $\rho_c(L, E) \ll \rho_B(L)$ , where  $\rho_c$  is the gyroradius of protons, and  
 87  $\rho_B$  is the radius of curvature of the magnetic field (near the equatorial plane). According to this  
 88 criterion and to the theory of stochastic motion of particles, the geomagnetic trap in the dipolar  
 89 region can capture and durably hold only protons with  $E \text{ (MeV)} < 2000 \cdot L^{-4}$  (Ilyin et al., 1984). The  
 90 green line in Fig. 1 represents this boundary.

91 The distribution of the ERB proton fluxes shown in Fig. 1, refer to the years of the solar  
 92 maximum, but the solar-cyclic variations in the ERB proton fluxes are small and localized at  $L <$   
 93  $2.5$  (mainly at  $L < 1.4$ ).

## 94 2.2 Spatial-energy distributions of the ERB protons outside the equatorial plane

95 The stationary fluxes  $J$  of the ERB particles with given energy and local pitch-angle  $\alpha$  decrease  
 96 usually when the point of observation is shifted from the equatorial plane to higher latitudes along  
 97 a certain magnetic field line. In the inner regions of the ERB, on  $L < 5$ , an angular distributions of  
 98 protons have usually a maximum at the local pitch-angle  $\alpha = 90^\circ$ . In wide interval near this  
 99 maximum these distributions are well described by the function  
 100  $J(\alpha, B/B_0) \propto (B/B_0)^{-A/2} \sin^A \alpha$  (Parker, 1957), where  $A$  is the index of an anisotropy of a  
 101 fluxes,  $B$  is the induction of a magnetic field at the point of measurements of these fluxes and  $B_0$  is  
 102 induction of a magnetic field at the equatorial plane on the same magnetic line.





104 **Figure 2.** Empirical model of the anisotropy index  $A(E, L)$  of the ERB proton fluxes averaged on the data of the  
105 satellites obtained near the plane of the geomagnetic equator. Values of  $A$  are given on iso-lines of the anisotropy:  $A =$   
106  $1.5\text{--}8.5$  with the step  $\Delta A = 0.5$ .

107 The generalized empirical model of an anisotropy  $A(E, L)$  for the proton fluxes with  $E \sim 0.1\text{--}2$   
108 MeV on  $L \sim 2\text{--}5$  near the equatorial plane for the stationary ERB ( $Kp < 2$ ) is presented in Fig. 2.  
109 The anisotropy index  $A$  of the proton fluxes is shown in Fig. 2, in the space  $\{E, L\}$ , in the form of  
110 iso-lines with the same values  $A$  from 1.5 to 8.0 and with a step  $\Delta A = 0.5$ . The integer values of  
111 this index are plotted on the corresponding iso-lines in red numbers.

112 When constructing this model, we consider and analyze the data of the following satellites:  
113 Explorer-12 (Hoffman and Bracken, 1965), Explorer-14 (Davis, 1965), Explorer-26 (Søraas and  
114 Davis, 1968), Electron (Ilyin et al., 1984; Vlasova et al., 1984), OV1-14 and OV1-19 (Fennell et  
115 al., 1974), Explorer-45 (Williams and Lyons, 1974; Fritz and Spjeldvik, 1981; Garcia and  
116 Spjeldvik, 1985), Molniya-1 (Vlasova et al., 1984), ISEE-1 (Garcia and Spjeldvik, 1985; Williams  
117 and Frank, 1984), SCATHA (Blake and Fennell, 1981), Van Allen Probes (Shi et al., 2016), and  
118 other satellites. These data were obtained in 1961-2015.

119 Figure 2 shows that for rather high energy ( $> 1$  MeV) the anisotropy of a proton fluxes  
120 monotonically increases with decreasing  $L$  (from  $A \sim 3.5$  to  $A \sim 8.0$ ). For  $E > 0.3$  MeV on  $L < 3$   
121 anisotropy is monotonically increases with increasing energy, but for  $E > 0.5$  MeV on  $L > 3$  it is  
122 almost independent on energy.

123 Some small irregularities of the iso-lines in Fig. 2 are connect to the fact that experimental data  
124 were used for constructing this figure; these data were obtained in different years, with different  
125 instruments on different orbits of satellites, and during different intensity of the solar activity. At  
126 the same time, Fig. 2 demonstrates the important regularities of the pitch-angle distributions of the  
127 stationary ERB protons.

128 In the region  $\{E > 0.5$  MeV,  $L > 3\}$  the iso-lines of the anisotropy index are almost parallel to  
129 each other and to the energy scale. This adiabatic regularity refers for protons belonging to the  
130 power-law tail of their energy spectra, the exponent of which practically does not change when  $L$   
131 changes (at  $L > 3$ ). In Fig. 2, the red lines correspond to the lower boundary of the power-law tail  
132 of the ERB protons energy spectra:  $E_b = (36 \pm 11) L^{-3}$  MeV (see Kovtyukh, 2001, 2020).

133 The pattern of  $A(E, L)$  in the region on  $L > 3$  at  $E \sim 0.2\text{--}0.5$  MeV and the local minimum at  $L \sim$   
134  $3$  ( $E \sim 0.2$  MeV) are connected with local maximum in the stationary proton energy spectra of the  
135 ERB which corresponds to  $E = (17 \pm 3) L^{-3}$  MeV (see Kovtyukh, 2001, 2020).

136 These regularities in the pattern of  $A(E, L)$  are explained within the framework of the theory of  
137 radial transport (diffusion) of the ERB protons with conservation of the adiabatic invariants  $\mu$  and  
138  $K$  of their periodic motions (these questions were most fully considered in Kovtyukh, 1993).

139 Local maximum at  $L \sim 2.5$  ( $E < 0.1$  MeV) and the region of low anisotropy at  $L \sim 2$  ( $E \sim 0.1$   
140 MeV) in Fig. 2, are connected with the ionization losses of protons.

141 High anisotropy for the fluxes of protons at  $E = 5\text{--}50$  MeV and a strong dependence  $A(L)$  at the  
142 inner boundary of the inner belt ( $L = 1.15\text{--}1.40$ ,  $B/B_0 = 1.0\text{--}1.7$ ) were obtained on the satellite  
143 DIAL (Fischer et al., 1977). According to these data, an anisotropy index increase from  $A \sim 12$  at  
144  $L = 1.25$  to  $A \sim 60$  at  $L = 1.15$ , and do not depends on  $L$  at  $L = 1.25\text{--}1.40$ . These results are supported  
145 by the data of the satellite Resurs-01-N4 for the protons with  $E = 12\text{--}15$  MeV which obtained at  
146  $h \sim 800$  km (Leonov et al., 2005). They will be taken into account in our calculations.

147 The experimental results on the pitch-angle distributions of the ERB proton fluxes and their  
148 anisotropy indexes were discussed in detail in (Kovtyukh, 2018).

### 149 **2.3 Drift frequency distributions of the ERB protons**

150 Based on the results shown in Fig. 1 and 2, one can calculate the distributions of the ERB protons  
151 over the drift frequency  $f_d$ . In these calculations, the dipole model of the geomagnetic field was



152 used, according to which (see, e. g., Roederer, 1970) the point of the magnetic field line at  
 153 geomagnetic latitude  $\lambda$  is located from the center of the dipole at a distance

$$154 \quad R(L, \lambda) = R_E L \cos^2 \lambda,$$

155 where  $R_E$  is the Earth's radius, and the field induction at a given  $L$  changes with changing  $\lambda$  as

$$156 \quad B(L, \lambda) = \frac{\sqrt{4 - 3 \cos^2 \lambda}}{\cos^6 \lambda} B_0(L),$$

157 where  $B_0(L) = 0.311 \text{ Gs} \times L^{-3}$ .

158 It was also taken into account that the drift frequency  $f_d$  of the nonrelativistic particles depends  
 159 essentially only on their kinetic energy  $E$  and on  $L$ . This value depends very slightly on the particle  
 160 pitch-angle: with an increase in the geomagnetic latitude of the mirror point of the particle trajectory  
 161 from 0 to  $10^\circ$  it increases by only 1.5%, and in the range from 0 to  $20\text{--}30^\circ$  it increases by 5.8–12.5%.

162 The number of protons with energies from  $E$  to  $E+dE$  per unit volume  $n$  is equal to the differential  
 163 flux of these particles  $J$  (falling per unit time per unit area of the detector per unit solid angle), divided  
 164 by the velocity  $v$  of these particles:  $n = J/v$ . For nonrelativistic protons with mass  $m$ , this velocity is  
 165  $(2E/m)^{1/2}$ .

166 Then in the near-equatorial region, between  $L$  and  $L+dL$  and within geomagnetic latitudes from  
 167 0 to  $\pm\lambda_0$ , the total number of nonrelativistic protons with mirror points within this region and with  
 168 energy from  $E$  to  $E+dE$ , drifting on a given  $L$  with frequency  $f_d(L, E)$  around the Earth, is

$$169 \quad \Delta N(L, f_d) = 2 \int_0^{\lambda_0} 2\pi R_E^2 L dL \frac{B_0(L)}{B(L, \lambda)} R_E L \cos \lambda \sqrt{4 - 3 \cos^2 \lambda} d\lambda \times$$

$$4\pi \int_{\alpha_{01}}^{\alpha_{02}} \frac{J(L, E(L, f_d)) dE}{\sqrt{2E(L, f_d)/m}} \sin^A \alpha_0 \cos \alpha_0 d\alpha_0,$$

170 where  $m$  is the rest mass of a proton,  $J(L, E(L, f_d))$  is the differential fluxes and  $E(L, f_d)$  is the protons  
 171 energy. The first integral takes into account that the magnetic flux in the layer between shells  $L$  and

172  $L+dL$  it conserved when latitude  $\lambda$  changes, i. e.  $2\pi R_E L \cos \lambda R_E dL = 2\pi R_E L \frac{B_0(L)}{B(L, \lambda)} R_E dL$ .

173 As result of integrating the last expression over  $\alpha_0$  and replacing  $\cos \lambda \equiv t$ , we obtain:

$$174 \quad \Delta N(L, f_d) = 4\pi R_E^3 L^2 dL \frac{J(L, E(L, f_d)) dE}{\sqrt{2E(L, f_d)/m}} \times \frac{4\pi}{A+1} \times$$

$$\int_{\cos \lambda_0}^1 t^7 \left[ \left( \frac{t^6}{\sqrt{4-3t^2}} \right)^{\frac{A+1}{2}} - (0.565)^{A+1} \right] dt.$$

175 When integrating over equatorial pitch-angles  $\alpha_0$ , Liouville's theorem and the conservation of  
 176 the first adiabatic invariant ( $\mu$ ) are taken into account:  $\sin^2 \alpha_{01} = B_0(L)/B(L, \lambda_0)$  and  $\sin^2 \alpha_{02} =$   
 177  $B_0(L)/B(L, \lambda)$ , where  $B(L, 0) = B_0(L)$ .

178 With an increase  $\lambda$  from 0 to  $\lambda_0 = 30^\circ$ , the value of the function  $\sqrt{4-3t^2}$  increases from 1 to  
 179 1.32, i.e. deviates from the average value (1.16) by only 16%. Most part of the ERB protons are



180 concentrated at these latitudes. Therefore, when calculating the last integral, we will assume that  
 181  $\sqrt{4-3t^2} \approx 1.16$ .

182 Then you can get the following expression:

183 
$$\Delta N(L, f_d) = k \frac{J(L, E(L, f_d))}{\sqrt{E(L, f_d)}} F(A) L^2 dL dE ,$$

184 where

185  
 186 
$$F(A) = \frac{1}{A+1} \left[ \frac{(1.16)^{-(A+1)/2}}{3A+11} (1-0.21 \cdot 0.65^A) - 0.085(0.565)^{A+1} \right]$$

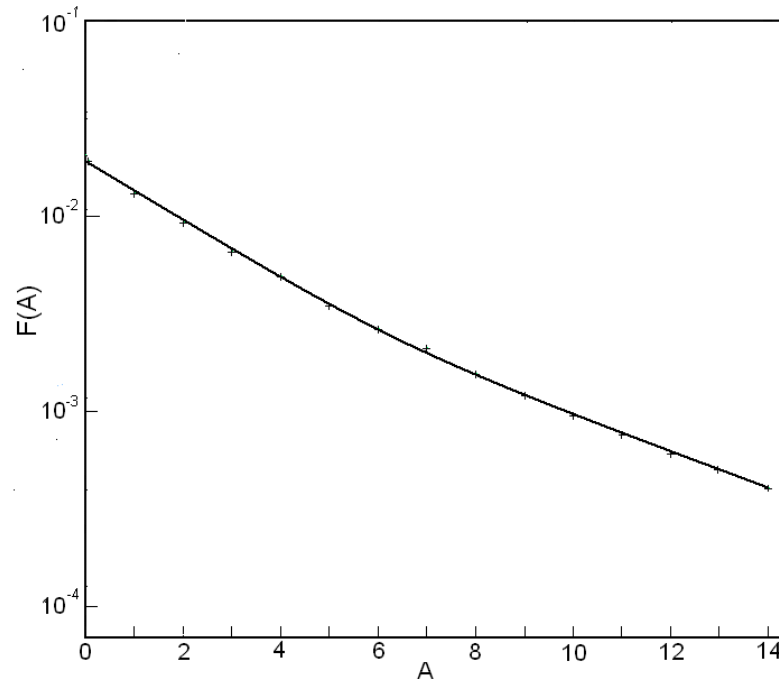
187 and

188 
$$k = (4\pi)^2 R_E^3 \sqrt{m/2} = 2.945 \cdot 10^{19} \text{ cm}^2 \text{ s sr MeV}^{1/2} .$$

189 When calculating the values of  $\Delta N$ , we will take that  $dL/L = dE/E = 0.1$ . Finally, for the  
 190 indicated ERB region near the equatorial plane, we obtain:

191 
$$\Delta N(L, f_d) = 2.945 \cdot 10^{17} J(L, E(L, f_d)) \sqrt{E(L, f_d)} F(A) L^3 , \quad (1)$$

192 where  $J$ , the differential fluxes of protons with equatorially pitch-angle  $\alpha_0 \approx 90^\circ$ , is given in units  
 193 of  $(\text{cm}^2 \text{ s sr MeV})^{-1}$ , and the energy of protons  $E$  is given in MeV. The dependence  $F(A)$  is shown  
 194 in Fig. 3.



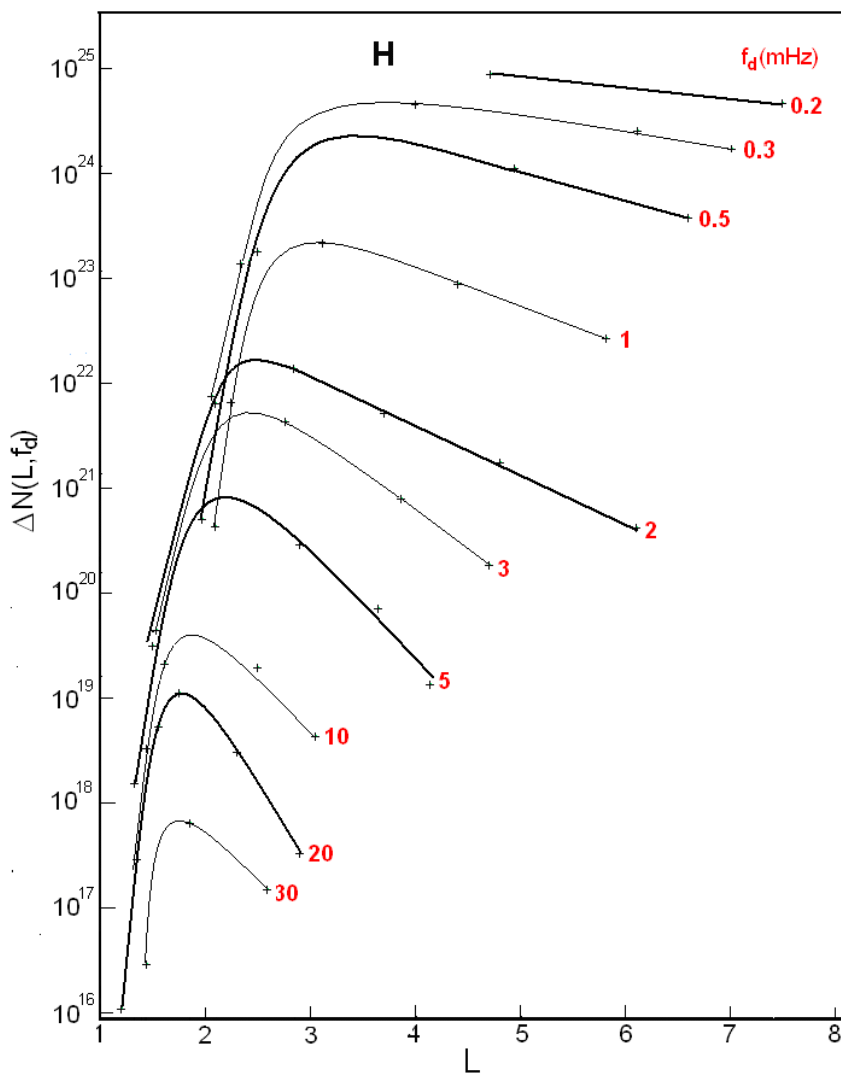
195

196 **Figure 3.** Dependence of the factor  $F(A)$  in formula (1) on the anisotropy index  $A$  of the proton fluxes.

197 For protons of the ERB, the radial profiles  $\Delta N(L, f_d)$  for  $f_d = 0.2, 0.3, 0.5, 1, 2, 3, 5, 10, 20$ , and  
 198 30 mHz, calculated by the formula (1) with using Figs. 1–3 are shown in Fig. 4, and the frequency  
 199 spectra  $\Delta N(f_d, L)$  at  $L = 2, 2.5, 3, 4, 5$ , and 6 are shown in Fig. 5. Near each curve in Fig. 4, the

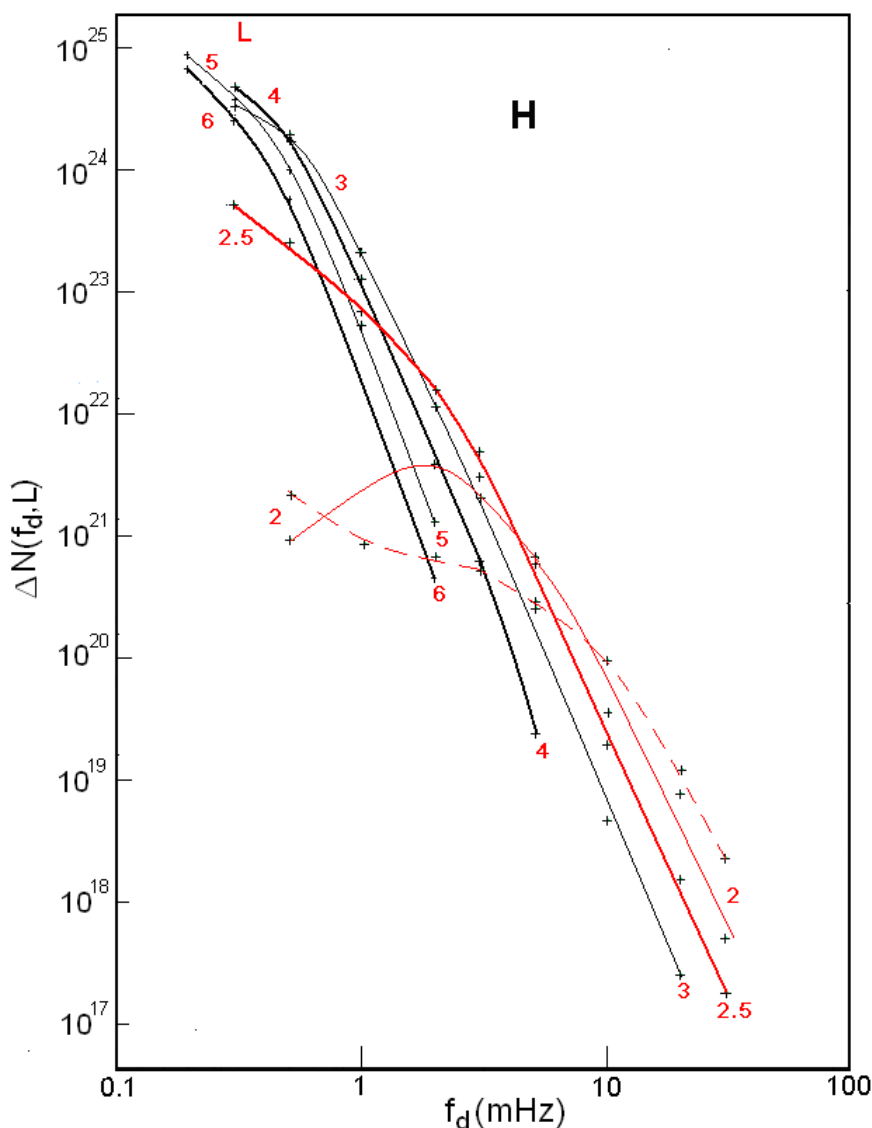


200 corresponding value of  $f_d$  (mHz) is indicated, and each spectrum in Fig. 5 have the corresponding  $L$   
201 value (these values are highlighted in red). For clarity, in Figs. 4 and 5, thin curves alternate with  
202 thick curves and in Fig. 5 spectra at  $L = 2$  and  $2.5$  are highlighted in red.



203  
204 **Figure 4.** Radial profiles  $\Delta N(L, f_d)$  for protons of the ERB with drift frequencies  $f_d = 0.2, 0.3, 0.5, 1, 2, 3, 5, 10, 20$  and  
205  $30$  mHz, plotted for periods of solar activity maxima. The  $f_d$  values corresponding to each curve are highlighted in red.  
206 For clarity, thin curves are interspersed with thick curves.





207  
 208 **Figure 5.** Frequency spectra  $\Delta N(f_d, L)$  for protons of the ERB at  $L = 2, 2.5, 3, 4, 5$  and  $6$ , plotted for periods of solar  
 209 activity maxima. The values  $L$  corresponding to each spectrum and spectra at  $L = 2$  and  $2.5$  are highlighted in red. The  
 210 red dotted line shows the spectrum  $\Delta N(f_d, L)$  of the ERB protons at  $L = 2$ , constructed from data for periods of solar  
 211 activity minima (see Kovtyukh, 2020). For clarity, thin curves are interspersed with thick curves.

212 The errors of these calculations consist mainly of the errors of the averaged experimental data  
 213 shown in Figs. 1 and 2 (these errors are most significant at  $L < 2$ ), and because of the deviations of  
 214 the geomagnetic field from the dipole model at  $L > 5$ .

215 As  $\lambda_0$  decreases, the errors in our calculations will decrease. These errors can be reduced also by  
 216 using numerical computer calculations. However, it should be taken into account that the fluxes of  
 217 the ERB protons, as well as the energy spectra and pitch-angle distributions of these fluxes, may  
 218 experience changes that exceed the errors of our calculations even in very quiet periods of  
 219 observations.

### 220 3 Discussion



221 In agreement with the results of experimental and theoretical studies, at  $L > 2.5$ , the main  
222 mechanism for the formation of the ERB for protons is the radial diffusion of particles from the  
223 outer boundary of the geomagnetic trap to the Earth under conservation the adiabatic invariants  $\mu$   
224 and  $K$  (see, e.g., Lejosne and Kollmann, 2020; Kovtyukh, 2016b, 2018).

225 Figures 1 and 2 presented here make it possible to determine in which regions of the space  
226  $\{E, L\}$  near the equatorial plane the ionization losses of ions during their radial diffusion can be  
227 neglected and where this cannot.

228 Iso-lines of the proton fluxes in Fig. 1 at sufficiently large  $E$  and  $L$  go up with decreasing  $L$ , in  
229 the direction of increasing energy, in strict agreement with the adiabatic laws of radial transport of  
230 particles. At lower  $L$  these iso-lines reject to the low energies, under the influence of ionization  
231 losses, which increase rapidly with decreasing  $L$  (see in Kovtyukh, 2020 for details).

232 At sufficiently large values of  $E$  and  $L$ , iso-lines of the anisotropy index in Fig. 2 pass  
233 practically parallel to each other and parallel to the energy axis, in agreement with the laws of  
234 adiabatic transport of particles with power-law energy spectra (see Kovtyukh, 1993). At lower  $E$   
235 and  $L$ , a more complex picture is formed under the influence of ionization losses (for more details  
236 see in Kovtyukh, 2001, 2018).

237 With decreasing  $L$ , the radial diffusion are decreased very rapidly, and the belt of protons with  $E$   
238  $> 10$ – $20$  MeV on  $L < 2$  is generated mainly as result of decay a neutrons of albedo which are  
239 knocked from the atmospheric atoms nuclei by the Galactic Cosmic Rays (GCR) protons. This  
240 mechanism (CRAND) is simulated in many contemporary studies based on the experimental data  
241 (see, e. g., Selesnick et al., 2007, 2013, 2014, 2018).

242 The mechanisms of formation of the ERB under the action of radial diffusion and CRAND are  
243 manifested and clearly differ both in the radial profiles  $\Delta N(L, f_d)$  and in the frequency spectra  
244  $\Delta N(f_d, L)$  of protons.

245 Let us consider the manifestations of these mechanisms in Fig. 4 and 5 and related effects.

246 In contrast to the radial profiles of fluxes  $J(L, E)$ , the radial profiles  $\Delta N(L, f_d)$  for protons with  $f_d$   
247  $> 10$  mHz (see Fig. 4) have much less steep of the outer edges and their steepness decreases with  
248 decreasing frequency  $f_d$ . This effect is connected mainly with an increase in the volume of  
249 magnetic tubes (factor  $L^3$  in formula (1) from Section 2.3) and with a decrease in the anisotropy  
250 index of proton fluxes with increasing  $L$ .

251 At the same time, in comparison with the radial profiles  $J(L, E)$ , the radial profiles  $\Delta N(L, f_d)$   
252 have more steeper inner edges. This effect is connect mainly with the large anisotropy of proton  
253 fluxes in the corresponding region of space  $\{E, L\}$  and with the rapid growth of the anisotropy  
254 index with decreasing  $L$  in this region. It is especially expressed in the radial profiles  $\Delta N(L, f_d)$  at  $f_d$   
255  $\sim 0.3$ – $1$  mHz (see Fig. 4); this is due to the fact that in the corresponding region of space  $\{E, L\}$  the  
256 anisotropy index of proton fluxes strongly depends on  $E$  and  $L$  (see Fig. 2).

257 Radial profiles  $\Delta N(L, f_d)$  at  $f_d > 10$  mHz are formed by the mechanism CRAND. They have a  
258 maximum at  $L \sim 1.5$ – $2.0$ , and the steepness of their inner and outer edges does not differ as much  
259 as for lower frequencies  $f_d$  (see Fig. 4). When constructing these profiles, it was taken into account  
260 that at  $E = 5$ – $50$  MeV an anisotropy index  $A$  of proton fluxes do not depend on  $L$  at  $L = 1.25$ – $1.40$ :  
261  $A = 12 \pm 2$  (Fischer et al., 1977; Leonov et al., 2005).

262 The shape of the spectra  $\Delta N(f_d, L)$  at  $L > 3$  is determined, first of all, by the shape of the energy  
263 spectra of proton fluxes  $J(E, L)$  at the outer boundary of the geomagnetic trap. Gradually, as the  
264 particles diffuse to the Earth, their energy spectra are transformed under the action of betatron  
265 acceleration and ionization losses of particles.

266 In contrast to the energy spectra of proton fluxes  $J(E, L)$ , distributions  $\Delta N(f_d, L)$  of the ERB  
267 protons over their drift frequency  $f_d$  (Fig. 5) differ much less from each other at  $L > 3$ . Such  
268 convergence of the spectra  $\Delta N(f_d, L)$  driven by increase in the volume of magnetic tubes and a



269 decrease in the anisotropy index of the ERB proton fluxes with increasing  $L$ . Figure 5 testify for  
270 close to adiabatic transformations of the spectra  $\Delta N(f_d, L)$  when  $L$  changes at  $L > 3$ .

271 The energy spectra of near-equatorial proton fluxes  $J(E, L)$  with  $E > 10 \cdot L^{-3}$  MeV at  $L > 3$  in  
272 quiet periods have a local maximum at  $E = (17 \pm 3) \cdot L^{-3}$  MeV and a power-law tail ( $J \propto E^{-\gamma}$ , where  $\gamma$   
273  $= 4.25 \pm 0.75$ ) at  $E > (36 \pm 11) \cdot L^{-3}$  (Kovtyukh, 2001, 2018, 2020).

274 The frequency spectra of the ERB protons at  $L > 3$  weakly depend on  $L$  and over the considered  
275 range  $\Delta f_d$  have a close to power-law shape with an exponent  $\gamma = 4.71 \pm 0.43$  (at  $f_d > f_d^*$ , where  $f_d^*$   
276  $\sim 0.5$  mHz at  $L \sim 3-6$ ,  $\sim 2$  mHz at  $L = 2.5$  and  $\sim 5$  mHz at  $L = 2$ ). Note that the spread of the  
277 parameter  $\gamma$  for the frequency spectra of protons is almost 2 times less than for their energy spectra.  
278 These spectra become more rigid (flattened) at  $f_d < f_d^*$ .

279 Thus, the average exponents of the power-law tail of the energy and frequency spectra of  
280 protons differ by  $\Delta\gamma = 0.46$ , and there is no local maximum in the frequency spectra at  $f_d > 2$  mHz  
281 at  $L > 2.5$ . The main role in such differences in the shape of the energy and frequency spectra of  
282 protons was played by the factor  $F(A)$  in formula (1), in which the anisotropy index  $A$  is a function  
283 of  $E$  and  $L$  (see Figs. 2 and 3). Note that in the region  $\{E > 0.5 \text{ MeV}, L > 3\}$  the anisotropy index  
284  $A$ , as well as the protons energy, is transformed according to adiabatic laws when  $L$  changes (see  
285 Fig. 2 and comments to it).

286 These results confirm our hypothesis about the ordering of the distributions of protons over  
287 their drift frequency  $f_d$  in the outer regions of the ERB, at  $L > 3$ , where most of the ERB protons  
288 are located and where the radial diffusion of protons overpowers their ionization losses.

289 At all  $L$ , the frequency spectra  $\Delta N(f_d, L)$  become more flat at small  $f_d$  and  $E$  under influence  
290 ionization losses. However, in the range of high  $f_d$  (from 3–5 mHz to 30 mHz), for protons with  
291 high energies and low ionization losses, the protons frequency spectra save a power-law tail even  
292 at  $L = 2$  (see Fig. 5).

293 For protons with  $f_d < 0.5$  mHz, which correspond to the ERB protons of the lowest energies,  
294 ionization losses lead to the same consequences at higher  $L$ -shells: the radial profiles  $\Delta N(L, f_d)$   
295 approach each other, and the spectra  $\Delta N(f_d, L)$  flatten out (see Figs. 4 and 5).

296 In the region of the steep inner edge of the radial distributions  $\Delta N(L, f_d)$ , spectra  $\Delta N(f_d, L)$  of the  
297 ERB protons gradually, with decreasing  $L$ , become increasingly rigid and rapidly diverge from  
298 each other (see Fig. 4 and 5). In the range of small  $f_d$  at  $L < 2.5$ , the connection between these  
299 distributions and the shape of the boundary energy spectra of protons is gradually lost.

300 These results indicate a violation of the order in the distributions of protons under the influence  
301 of ionization losses.

302 In Fig. 5, the dotted line also shows the spectrum  $\Delta N(f_d, L)$  of the ERB protons at  $L = 2$ ,  
303 constructed from experimental data for periods of low solar activity (see Fig. 1 in Kovtyukh,  
304 2020). Figure 5 show that at  $L = 2$  for  $f_d > 10$  mHz there were more protons at the minimum of  
305 solar activity, and for  $f_d \sim 1-10$  mHz there were more protons at the maximum of solar activity.

306 The effect of a decrease in the  $\Delta N(f_d, L)$  values for protons with  $f_d > 10$  mHz at  $L < 2$  with an  
307 increase in solar activity is mainly connected with a decrease in the fluxes of protons with  $E > 10-$   
308  $20$  MeV here. This effect is well known. It is described by the CRAND mechanism (see, e.g.,  
309 Selesnick et al., 2007) and was considered in detail in (Kovtyukh, 2020). With an increase in solar  
310 activity, the densities of atmospheric atoms and ionospheric plasma on small  $L$ -shells significantly  
311 increase, which leads to an increase in ionization losses of the ERB protons, but the power of their  
312 main source (CRAND) practically does not change. As a result, the equilibrium fluxes and  $\Delta N(f_d,$   
313  $L)$  for protons with  $f_d > 10$  mHz are establish at lower levels.



314 However, the effect of an increase in  $\Delta N(f_d, L)$  for  $f_d \sim 1\text{--}10$  mHz at low  $L$  with increasing solar  
315 activity, corresponding to the protons of lower energies, was discovered here for the first time.

316 With decreasing in  $E$  (and  $f_d$ ) of protons their ionization losses increase, and if the fluxes of  
317 low-energy protons in the inner belt were also formed by the CRAND mechanism, one would have  
318 observe even stronger increase of their fluxes with solar activity decreasing, than for protons with  
319  $E > 10\text{--}20$  MeV ( $f_d > 10$  mHz). But for protons with  $f_d \sim 1\text{--}10$  mHz, we see in fig. 5 reverse effect  
320 in the spectra  $\Delta N(f_d, L)$  at  $L = 2$ , which is not described by the CRAND mechanism.

321 On the other hand, it was proved that stationary fluxes of protons with  $E < 15$  MeV at  $L \sim 2$  are  
322 formed mainly by the mechanism of protons radial diffusion from the external region of the ERB  
323 (Selesnick et al., 2007, 2013, 2014, 2018). These fluxes and  $\Delta N(f_d, L)$  values for  $f_d \sim 1\text{--}10$  mHz at  
324  $L = 2$  are formed as a result of a balance of competing processes radial diffusion of protons and  
325 their ionization losses.

326 The rates of transport of the ERB protons to the Earth (radial diffusion) rapidly increase with  
327 decreasing particles energy (see Kovtyukh, 1916b). In addition, with an increase in solar activity,  
328 the average level of geomagnetic fluctuations in the ERB increases. Under influence of these  
329 factors, one can expect a significant increase in the intensity of radial diffusion of the low-energy  
330 protons at low  $L$  with an increase in solar activity. As a result, the effect of increasing in the  
331 density of a dissipative medium with an increase in solar activity overpowered by a more  
332 significant effect of increasing in the rates of radial diffusion of protons.

333 According to a numerous experimental data, during magnetic storms complex and varied  
334 spectra of powerful pulsations of magnetic and electric fields in the frequency range considered  
335 here (ULF) can be generate in the geomagnetic trap, which are non-regular distributed over  $L$ ;  
336 these pulsations can lead to local acceleration and losses of the ERB particles (see, e.g., Sauvaud et  
337 al., 2013). Such effects will violate the regular character of the protons distributions shown in Fig.  
338 4 and 5. However, in quiet periods, the amplitudes of such pulsations are small and they lead only  
339 to radial diffusion of particles.

## 340 4 Conclusions

341 On the basis of generalized data on the fluxes of near-equatorial protons of the ERB with energy  
342 from  $E \sim 0.2$  MeV to 100 MeV at drift shells  $L$  from  $\sim 1$  to 8, the stationary distributions of the  
343 ERB protons over the drift frequency of particles around the Earth ( $f_d$ ) were constructed. The  
344 results of calculations of the number of protons  $\Delta N$  of the ERB within  $30^\circ$  in geomagnetic latitude  
345 at different  $L$  and  $f_d$  for periods of solar activity maximum are presented. They differ from the  
346 corresponding distributions of the ERB protons for periods of low solar activity only at  $L < 2.5$  (for  
347 comparison, the spectra of these distributions are given at  $L = 2$ ).

348 The radial profiles of these distributions  $\Delta N(L, f_d)$  have one maximum that shift toward the  
349 Earth with increasing  $f_d$ . In compare to the proton fluxes profiles  $J(L, E)$ , the radial profiles  $\Delta N(L,$   
350  $f_d)$  at  $f_d < 5$  mHz have steeper inner edges and flatter outer edges. However, the radial profiles  
351  $\Delta N(L, f_d)$  at  $f_d > 10$  mHz, which are formed by the CRAND mechanism, have inner and outer edges  
352 with only slightly difference from each other in the steepness.

353 In contrast to the energy spectra of proton fluxes  $J(E, L)$ , the frequency spectra  $\Delta N(f_d, L)$  of the  
354 ERB protons at  $L > 3$  are weakly depend on  $L$  and, for sufficiently large  $f_d$  they have a nearly  
355 power-law form with an exponent  $\gamma = 4.71 \pm 0.43$ . There is no local maximum in these spectra in  
356 the region  $\{f_d > 2 \text{ mHz}, L > 2.5\}$ , as in the corresponding  $J(E, L)$  spectra.

357 Distributions  $\Delta N(L, f_d)$  and  $\Delta N(f_d, L)$  of the ERB protons in the region  $\{f_d > 0.5 \text{ mHz}, L > 3\}$   
358 have a more orderly form than in the corresponding region of the space  $\{E, L\}$ , and the main  
359 physical processes in the ERB manifested more clearly in these distributions. In these region most



360 of the ERB protons are located and the radial diffusion of protons overpowers their ionization  
361 losses during the transport of particles to the Earth.

362 In the region of the steep inner edges of the radial distributions  $\Delta N(L, f_d)$ , the spectra  $\Delta N(f_d, L)$   
363 of protons rapidly diverge from each other with decreasing  $L$ , and at low frequencies these spectra  
364 become flatten. These results indicate a violation of the order in these distributions of protons  
365 under the influence of ionization losses.

366 With increasing in solar activity, the number of protons  $\Delta N(f_d, L)$  at  $L \sim 2$  decreases for  $f_d > 10$   
367 mHz and increases for  $f_d \sim 1-10$  mHz. The effect at high  $f_d$ , corresponding to protons with  $E > 15$   
368 MeV, is well known and is described in the framework of the CRAND mechanism.

369 However, the opposite effect, at low  $f_d$  corresponding to the lower-energy protons, is discovered  
370 here for the first time. This effect can be associated with the fact that the low-frequency part of the  
371 spectrum  $\Delta N(f_d, L)$  of protons, even at  $L \sim 2$ , is formed mainly by the mechanism of protons  
372 transport from the outer regions of the ERB. This effect may indicate that with increasing of the  
373 solar activity, the average rates of radial diffusion of protons increase also. For low-energy protons  
374 at  $L \sim 2$ , the effect of increasing density of a dissipative medium with increasing solar activity  
375 overpowered by increasing the rates of radial diffusion of particles.  
376

377 *Data availability.* All data from this investigation are presented in Figs. 1–5.

378 *Competing interests.* The author declares that there is no conflict of interest.

379 *Acknowledgements.* The author would like to thank the reviewers.

380

381



## 382 References

- 383 Alfvén, H., and Fälthammar, C.-G.: *Cosmical Electrodynamics, Fundamental Principles*,  
384 Clarendon Press, Oxford, 1963.
- 385 Davis, L. R.: Low energy trapped protons and electrons, *Proc. Plasma Space Sci. Symp.*, Eds. D.  
386 B. Chang and C. Y. Huang, Washington, P. 212–226, 1965.
- 387 Fennell, J. F., Blake, J. B., and Paulikas, G. A.: Geomagnetically trapped alpha particles, 3. Low-  
388 altitude outer zone alpha-proton comparisons, *J. Geophys. Res.*, **79**(4), 521–528,  
389 <https://doi.org/10.1029/JA079i004p00521>, 1974.
- 390 Fischer, H. M., Auschrat, V. W., and Wibberenz, G.: Angular distribution and energy spectra of  
391 protons of energy  $5 \leq E \leq 50$  MeV in the lower edge of the radiation belt in equatorial latitudes,  
392 *J. Geophys. Res.*, **82**(4), 537–547, <https://doi.org/10.1029/JA082i004p00537>, 1977.
- 393 Fritz, T. A., and Spjeldvik, W. N.: Steady-state observations of geomagnetically trapped energetic  
394 heavy ions and their implications for theory, *Planet. Space Sci.*, **29**(11), 1169–1193,  
395 [https://doi.org/10.1016/0032-0633\(81\)90123-9](https://doi.org/10.1016/0032-0633(81)90123-9), 1981.
- 396 Garcia, H. A., and Spjeldvik, W. N.: Anisotropy characteristics of geomagnetically trapped ions, *J.*  
397 *Geophys. Res.*, **90**(A1), 359–369, <https://doi.org/10.1029/JA090iA01p00359>, 1985.
- 398 Hoffman, R. A., and Bracken, P. A.: Magnetic effects of the quiet-time proton belt, *J. Geophys.*  
399 *Res.*, **70**(15), 3541–3556, <https://doi.org/10.1029/JZ070i015p03541>, 1965.
- 400 Ilyin, B. D., Kuznetsov, S. N., Panasyuk, M. I., and Sosnovets, E. N.: Non-adiabatic effects and  
401 boundary of the trapped protons in the Earth's radiation belts, *Bulletin of the Russian Academy*  
402 *of Sciences: Physics*, **48**(11), 2200–2203, 1984.
- 403 Kovtyukh, A. S.: Relation between the pitch-angle and energy distributions of ions in the Earth's  
404 radiation belts, *Geomagn. Aeron.*, **33**(4), 453–460, 1993.
- 405 Kovtyukh, A. S.: Geocorona of hot plasma, *Cosmic Res.*, **39**(6), 527–558,  
406 <https://doi.org/10.1023/A:1013074126604>, 2001.
- 407 Kovtyukh, A. S.: Radial dependence of ionization losses of protons of the Earth's radiation belts,  
408 *Ann. Geophys.*, **34**(1), 17–28, <https://doi.org/10.5194/angeo-34-17-2016>, 2016a.
- 409 Kovtyukh, A. S.: Deduction of the rates of radial diffusion of protons from the structure of the  
410 Earth's radiation belts, *Ann. Geophys.*, **34**(11), 1085–1098, [https://doi.org/10.5194/angeo-34-](https://doi.org/10.5194/angeo-34-1085-2016)  
411 [1085-2016](https://doi.org/10.5194/angeo-34-1085-2016), 2016b.
- 412 Kovtyukh, A. S.: Ion Composition of the Earth's Radiation Belts in the Range from 100 keV to  
413 100 MeV/nucleon: Fifty Years of Research, *Space Sci. Rev.*, **214**(8), 124:1–124:30,  
414 <https://doi.org/10.1007/s11214-018-0560-z>, 2018.
- 415 Kovtyukh, A. S.: Earth's radiation belts' ions: patterns of the spatial-energy structure and its solar-  
416 cyclic variations, *Ann. Geophys.*, **38**(1), 137–147, doi:10.5194/angeo-38-137-2020, 2020.
- 417 Lejosne, S., and Kollmann, P.: Radiation Belt Radial Diffusion at Earth and Beyond, *Space Sci.*  
418 *Rev.*, **216**(1), 19:1–19:78, <https://doi.org/10.1007/s11214-020-0642-6>, 2020.
- 419 Leonov, A., Cyamukungu, M., Cabrera, J., Leleux, P., Lemaire, J., Gregorie, G., Benck, S.,  
420 Mikhailov, V., Bakaldin, A., Galper, A., Koldashov, S., Voronov, S., Casolino, M., De Pascale,  
421 M., Picozza, P., Sparvolli, R., Ricci, M.: Pitch-angle distribution of trapped energetic protons  
422 and helium isotop nuclei measured along the Resurs-01 No.4 LEO satellite, *Ann. Geophys.*,  
423 **23**(8), 2983–2987, <https://doi.org/10.5194/angeo-23-2983-2005>, 2005.
- 424 Northrop, T. G.: *The Adiabatic Motion of Charged Particles*, Wiley-Interscience, NY, USA, 1963.
- 425 Parker, E. N.: Newtonian development of the dynamical properties of ionized gases of low density,  
426 *Phys. Rev.*, **107**(4), 924–933. <https://doi.org/10.1103/PhysRev.107.924>, 1957.
- 427 Roederer, J. G.: *Dynamics of Geomagnetically Trapped Radiation*, Springer, NY, USA, 1970.
- 428 Sauvaud, J.-A., Walt, M., Delcourt, D., Benoist, C., Penou, E., Chen, Y., and Russell C. T.: Inner  
429 radiation belt particle acceleration and energy structuring by drift resonance with ULF waves





- 430 during geomagnetic storms, *J. Geophys. Res. Space Physics*, **118**(4), 1723–1736,  
431 <https://doi.org/10.1002/jgra.50125>, 2013.
- 432 Selesnick, R. S., Looper, M. D., and Mewaldt, R. A.: A theoretical model of the inner proton  
433 radiation belt, *Space Weather*, **5**(4), S04003, <https://doi.org/10.1029/2006SW000275>, 2007.
- 434 Selesnick, R. S., Hudson, M. K., and Kress B. T.: Direct observation of the CRAND proton  
435 radiation belt source, *J. Geophys. Res. Space Phys.*, **118**(12), 7532–7537,  
436 <https://doi.org/10.1002/2013JA019338>, 2013.
- 437 Selesnick, R. S., Baker, D. N., Jaynes, A. N., Li, X., Kanekal, S. G., Hudson, M. K., and Kress, B.  
438 T.: Observations of the inner radiation belt: CRAND and trapped solar protons, *J. Geophys.  
439 Res. Space Phys.*, **119**(8), 6541–6552, <https://doi.org/10.1002/2014JA020188>, 2014.
- 440 Selesnick, R. S., Baker, D. N., Kanekal, S. G., Hoxie, V. C., and Li, X.: Modeling the proton  
441 radiation belt with Van Allen Probes Relativistic Electron-Proton Telescope data, *J. Geophys.  
442 Res. Space Phys.*, **123**(1), 685–697, <https://doi.org/10.1002/2017JA024661>, 2018.
- 443 Shi, R., Summers, D., Ni, B., Manweiler, J. W., Mitchell, D. G., and Lanzerotti, L. J.: A statistical  
444 study of proton pitch-angle distributions measured by the Radiation Belt Storm Probes Ion  
445 Composition Experiment, *J. Geophys. Res. Space Phys.*, **121**(6), 5233–5249,  
446 <https://doi.org/10.1002/2015JA022140>, 2016.
- 447 Søråas, F., and Davis, L.R.: Temporal variations of 100 keV to 1700 keV trapped protons observed  
448 on satellite Explorer 26 during first half of 1965, Rep. X-612-68-328, NASA Goddard Space  
449 Flight Cent., Greenbelt, Md., 1968.
- 450 Vlasova, N. A., Kuznetsov, S. N., Panasyuk, M. I., and Sosnovets, E. N.: Anisotropy of protons  
451 and heavy ions in the Earth's radiation belts, *Bulletin of the Russian Academy of Sciences:  
452 Physics*, **48**(11), 2204–2207, 1984.
- 453 Williams, D. J., and Lyons, L. R.: The proton ring current and its interaction with plasmopause:  
454 Storm recovery phase, *J. Geophys. Res.*, **79**(28), 4195–4207,  
455 <https://doi.org/10.1029/JA079i028p04195>, 1974.
- 456 Williams, D. J., and Frank, L. A.: Intense low-energy ion populations at low equatorial altitude, *J.  
457 Geophys. Res.*, **89**(A6), 3903–3911, <https://doi.org/10.1029/JA089iA06p03903>, 1984.
- 458